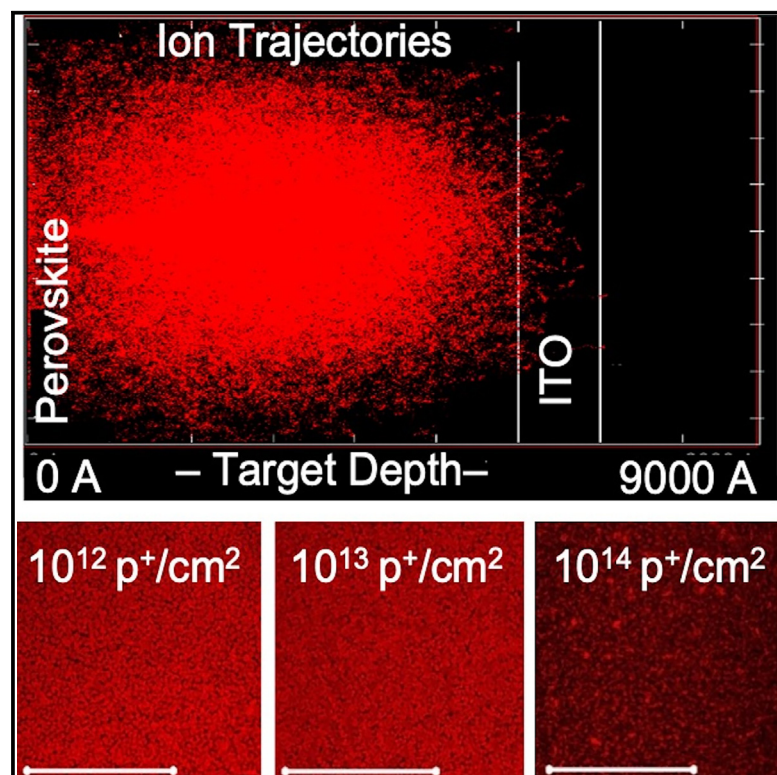# Elucidating early proton irradiation effects in metal halide perovskites via photoluminescence spectroscopy

Graphical abstract

Authors

Samuel Erickson, Calista Lum,
Katie Stephens, ..., Timothy J. Peshek,
Lyndsey McMillon-Brown,
Sayantani Ghosh

Correspondence

sghosh@ucmerced.edu

In brief

Physics; Materials science; Energy materials

Highlights

- First study of neutron and proton irradiation on unencapsulated perovskite films

- Proton irradiation > 10^{13}/cm^2 causes 30% darkening and shorter recombination lifetimes

- Photoluminescent spectroscopy reveals damage earlier than electrical measurements

CellPress

Article

Elucidating early proton irradiation effects in metal halide perovskites via photoluminescence spectroscopy

Samuel Erickson,[1] Calista Lum,[1] Katie Stephens,[2] Mritunjaya Parashar,[3] Darshpreet Kaur Saini,[3] Bibhudutta Rout,[3] Cheol Park,[4] Timothy J. Peshek,[5] Lyndsey McMillon-Brown,[5] and Sayantani Ghosh[1,6,*]

[1]Department of Physics, University of California, Merced, Merced, CA, USA
[2]Materials and Biomaterials Science and Engineering, University of California, Merced, Merced, CA, USA
[3]Department of Physics, University of North Texas, Denton, TX, USA
[4]Advanced Materials and Processing Branch, NASA Langley Research Center, Hampton, VA 23681, USA
[5]Photovoltaic and Electrochemical Systems Branch, John H. Glenn Research Center, National Aeronautics and Space Administration, Cleveland, OH, USA
[6]Lead contact
*Correspondence: sghosh@ucmerced.edu
https://doi.org/10.1016/j.isci.2024.111586

SUMMARY

Metal halide perovskite (MHP) solar cells are promising aerospace power sources given their potential as inexpensive, lightweight, and resilient solar electricity generators. Herein, the intrinsic radiation tolerance of unencapsulated methylammonium lead iodide/chloride ($CH_3NH_3PbI_{3-x}Cl_x$) films was isolated. Spatially resolved photoluminescence (PL) spectroscopy and confocal microscopy revealed the fundamental defect physics through optical changes as films were irradiated with 4.5 MeV neutrons and 20 keV protons at fluences between 5×10^{10} and 1×10^{16} p$^+$/cm^2. As proton radiation increased beyond 1×10^{13} p$^+$/cm^2, defects formed in the film, causing both a decrease in photoluminescence intensity and a 30% increase in surface darkening. All proton irradiated films additionally exhibited continuous increase of energy bandgaps and decreasing charge recombination lifetimes with increasing proton fluences. These optical changes in the absorber layer precede performance declines detectable in standard current-voltage measurements of complete solar cell devices and therefore have the potential of serving as early indicators of radiation tolerance.

INTRODUCTION

Efficiency, reliability, and cost are critical in determining photovoltaic technologies for powering the commercialization of low Earth orbit (LEO). Metal halide perovskite (MHP) solar cells show promise as inexpensive, lightweight, and durable solar electricity sources for space applications.[1,2] The high-power conversion efficiencies, now exceeding 26% for single-junction MHP cells, and approaching 30% for perovskite-silicon tandems, rival technologies used currently on satellites.[3] Their tunable bandgap via composition changes also makes MHPs viable for multi-junction architectures to utilize more of the solar spectrum. They have additionally demonstrated exceptionally high specific power, reaching 29.4 W/g in recent reports, outperforming all other photovoltaic technologies.[4] However, deployment of any solar cell in the harsh space environment will require resilience to extreme temperatures, radiation, ultrahigh vacuum, and mechanical stresses. On airless bodies such as the Moon and Mars, daytime temperatures reach over $100°C$, while nights plummet below $-150°C$.[5] In addition to this dramatic thermal cycling, they will be exposed to AM0 radiation with high ultraviolet spectral weight and the full spectrum of the solar wind, en-

ergetic galactic cosmic rays, and sporadic solar particle events supplying high doses of ionizing radiation.[2,6,7]

In addition to protons, neutrons pose threats to solar power systems deployed in space. Though lower in intensity than trapped protons, high-energy neutrons generate cumulative damage via secondary ionizations and nuclear transmutations that degrade cell efficiency over operational lifetimes.[8] The lunar regolith generates a complex radiation environment. Neutron production first occurs when galactic cosmic ray protons collide and interact with the lunar regolith.[9] These energetic "fast" neutrons have the potential to cause permanent displacement damage upon colliding with atoms in solar cells or electronic components. Over time, successive collisions enable the high-speed neutrons to thermalize to lower energy "slow" neutrons (<0.4 eV) which then may induce shallow charge carrier traps before capture.[10–12] α-particles and electrons are parts of cosmic radiation as well, but both pose lower damage potential than protons on account of the former's low fluence and the latter's low mass.[13]

Prior research on MHP solar cells in controlled laboratory conditions hints at promising radiation resilience and minimal UV degradation without oxygen or moisture exposure.[14,15] Proton (p$^+$) fluences between 10^{12} and 10^{14} p$^+$/cm^2 have been reported
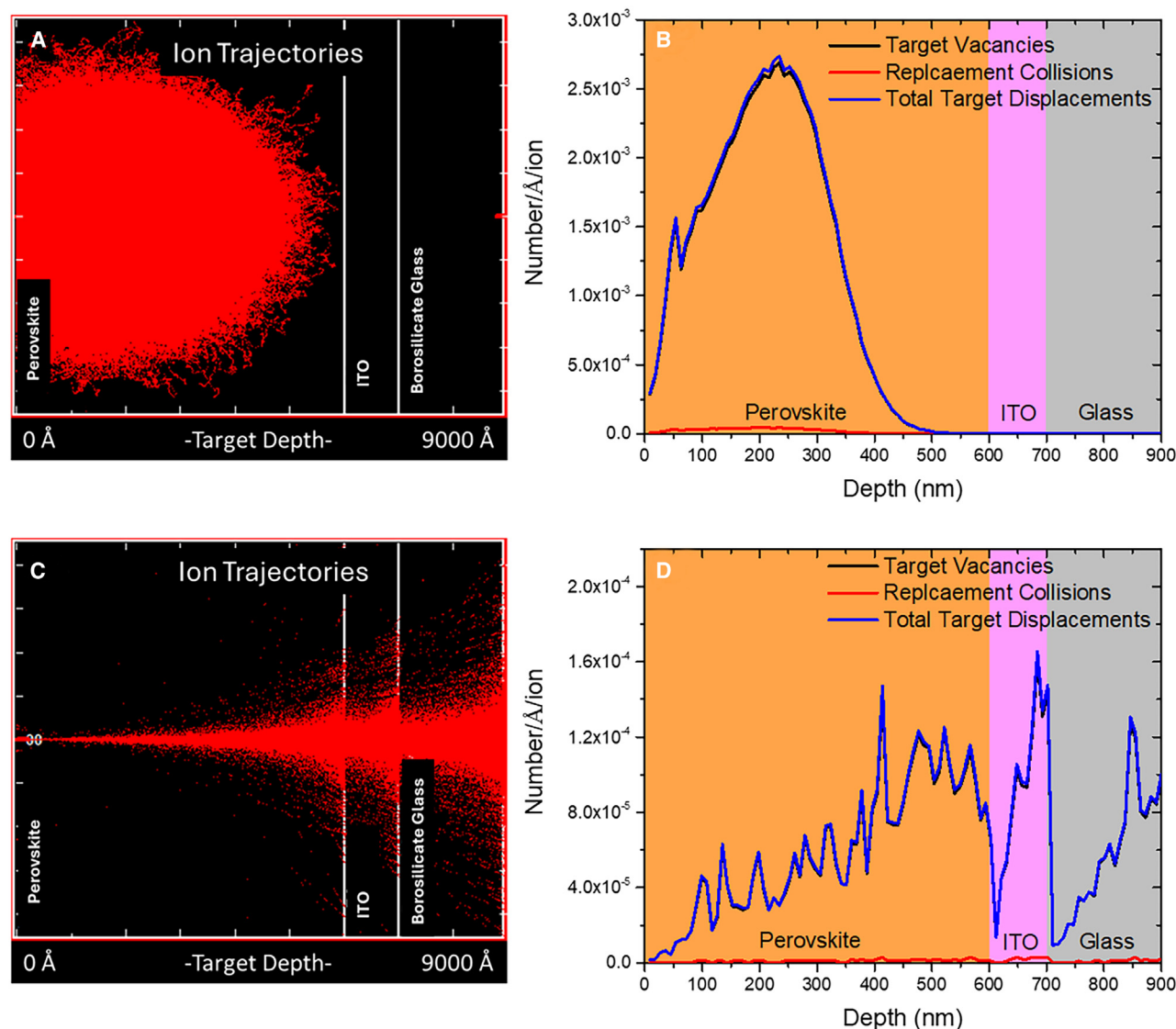
Figure 1. Determining proton beam energy

SRIM/TRIM simulations depicting (A) 20 keV and (C) 1 MeV proton trajectories within irradiated samples. The total stack consists of a 600 nm MHP film and a 300 nm ITO/glass substrate. Damage events due to 20 keV (B) and 1 MeV (D) energy protons as they move through the target layer.

as a minimum degradation threshold for MHP cells and bare perovskite films.[16–18] However, some open questions remain regarding real-world performance in space. For example, thermal cycling tends to reduce power conversion efficiency and accelerated light-induced damage occurs under vacuum environments.[19,20] Just a handful of brief sub-orbital space tests on encapsulated devices show persistent functionality but cannot fully validate long-duration orbital robustness.[21–23] Additionally, full-cell measurements make it difficult to pinpoint whether changes originate in the MHP layer itself or other cell components. In our prior work, we focused on intrinsic degradation pathways in the absorber layer alone to qualify operational lifetimes under LEO conditions where an encapsulated $CH_3NH_3PbI_3$ film was flown on the International Space Station (ISS) for 10 months[24]

The results were very encouraging; the sample was thermo-chemically stable, withstanding the repeated and rapid thermal cycling and AM0 exposure robustly, as supported by extensive post-flight characterization. The one question we were unable to address was the impact of radiation on the MHP film. The dominating radiation at the ISS constitutes protons estimated at a fluence of 10^9 cm^{-2} for the 10-month period. Simulations predicted that protons in the relevant energy range (0.05–10 MeV) would stop at the glass/encapsulant boundary before reaching the MHP film and roughening and discoloration of the interface between the glass and the encapsulant of the flight sample confirmed this. The MHP film was therefore entirely protected from radiation, and while this approach of hard encapsulation may ward off cosmic radiation induced degradation in MHP solar

20 keV Protons
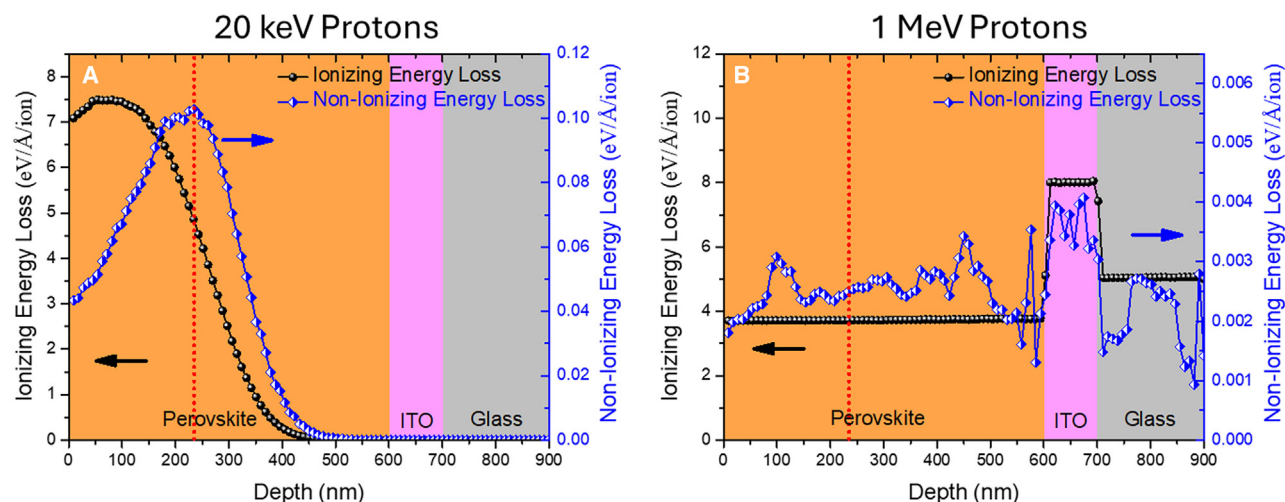
1 MeV Protons

Figure 2. IEL vs. NIEL
Ionizing energy loss (IEL) and non-ionizing energy loss (NIEL) were calculated via SRIM/TRIM simulations for (A) 20 keV and (B) 1 MeV protons in the perovskite/ITO/glass stack.

cells in the space environment, it would negate the significant advantages of *in situ* fabrication and low specific power that MHPs possess.[25]

In this work, we directly probed the MHP light-absorbing layer without any other interfaces or encapsulation and extracted fundamental insights on intrinsic radiation tolerance. We fabricated thin films of MHP with composition $CH_3NH_3PbI_{3-x}Cl_x$ (x = 0.15) on glass substrates and exposed them to controlled irradiation from a 4.5 MeV neutron (n^0) source and a 20 keV proton (p^+) beam at cumulative fluences ranging from 5×10^{10} to 1×10^{16} p^+/cm^2. Chloride concentrations <19% in the perovskite lattice have been shown to increase stability and favorably shift bandgap for photovoltaics.[26,27] We characterized the radiation damage effects in these bare films using spatially resolved photoluminescence (PL) spectroscopy to probe electronic structure and defect states and confocal fluorescence microscopy to map emitted intensity. While neutron irradiation appeared to have no effect on the films, higher proton irradiation fluences introduced greater numbers of defects into the normally highly emissive MHP lattice, causing observable optical changes even with no excess carriers injected as in standard electrical tests. Specifically, our PL data revealed decreasing emission intensity and thus escalating non-radiative pathways with increasing proton exposure, eventually darkening an additional 45% of the film area when fluence exceeds 1×10^{16} p^+/cm^2. All proton irradiated samples also exhibited gradual blue-shifting of optical bandgaps and shortening of photogenerated charge carrier lifetimes as proton fluence increased. Together these optical markers demonstrated escalating defect densities within the films resulting from collateral radiation damage.[18] This work is impactful because it is imperative that we understand the combined effects of stressors on perovskite-based photovoltaics in operation in space. Further, this investigation is the first of its kind to methodically investigate the impact of fast and slow neutrons with the most relevant proton energies directly applied to the absorber layer, and not constituent layers, to directly probe the

radiation resilience and degradation modes of unencapsulated perovskite films through optical analysis.

RESULTS

Determining proton beam energy

Prior radiation studies have shown the promising resilience of MHP solar cell devices under proton irradiation. The proton energy used has ranged from 150 keV to 10 MeV (mimicking typical LEO conditions) and in some cases even as high as 68 MeV.[14,28,29] These typically showed no radiation-induced irreversible damage, because while it is standard to qualify Si and III-V cells for use in space with high energy (>1 MeV) protons, such energy is inappropriate for MHP solar cells. These protons transfer very little energy to the thin MHP layers and even show signs of healing defects through ionization. A more appropriate range is 0.05–0.15 MeV, where protons stop inside the thin absorber layer, and in which cases vacancy and interstitial defect formation were observed.[30]

Nearly all prior research has used device stacks, including charge transport layers and electrodes, and sometimes, additional encapsulation layers and utilized the standard photovoltaic metrics, including short circuit current, open circuit voltage, fill factor, and power conversion efficiency (PCE), to evaluate radiation resistance.[16,18] To directly probe radiation tolerance of the light-absorbing layer itself, in this study we used methylammonium lead iodide/chloride ($CH_3NH_3PbI_{3-x}Cl_x$) perovskite films, of approximate thickness 600 nm, deposited onto indium tin oxide (ITO) coated glass substrates by spin-coating. Being a conducting surface, ITO could lead to some PL quenching. Despite this possibility, we used ITO as the substrate because a realistic device stack is almost certain to do so. As we have systematically utilized identical substrates for all our samples, this consistency ensures the relative differences observed in our samples with varying radiation flux and exposure remain valid. This simple structure omits all other device layers, allowing

Table 1. Irradiated samples included in the study

| Sample# | Irradiation (cm^{-2}) | | |
	First	Second	Third
1	low n^0	–	–
2	high n^0	–	–
3	low n^0	5×10^{10} p$^+$	1×10^{13} p$^+$
4	low n^0	1×10^{12} p$^+$	1×10^{14} p$^+$
5	5×10^{10} p$^+$	1×10^{13} p$^+$	–
6	1×10^{12} p$^+$	1×10^{14} p$^+$	–
7	5×10^{10} p$^+$	1×10^{13} p$^+$	–
8	1×10^{12} p$^+$	1×10^{14} p$^+$	–
9	1×10^{15} p$^+$	–	–
10	1×10^{16} p$^+$	–	–
11	1×10^{15} p$^+$	–	–
12	1×10^{16} p$^+$	–	–

All samples are unencapsulated $CH_3NH_3PbI_{3-x}Cl_x$ on ITO-coated glass. A control without radiation was also fabricated for each irradiation batch (first – third).

the characterization of the intrinsic absorber response without convoluting effects. For the selection of the appropriate proton energies for achieving representative defect generation, we used Stopping and Range of Ions in Matter (SRIM) and Transport of Ions in Matter (TRIM) simulations and found that 20 keV protons fell right in the middle of the perovskite absorber layer and produced the most uniform damage profile within our region of interest in the 600 nm thick films. These ion trajectory simulations, as well as their corresponding collision plots, are presented in Figure 1 for 20 keV and 1 MeV proton beam. As anticipated, while the 20 keV protons stop almost entirely within the absorber MHP layer (Figure 1A), 1 MeV protons interact very little with the MHP film (Figure 1C), confirming that low energy protons will maximize lattice displacements and vacancies due to the collisions. This is clear in Figures 1B and 1D, where 20 keV protons collide more uniformly and in much greater numbers than 1 MeV protons.

### Ionizing energy loss and non-ionizing energy loss

As the energetic proton beam penetrates through the target, it undergoes energy loss characterized by two processes: elastic collision with the nucleus, known as non-ionizing energy loss (NIEL), and inelastic collision with the electrons known as ionizing energy loss (IEL). Figure 2 shows the SRIM/TRIM simulated IEL and NIEL values for 20 keV and 1 MeV protons. From the structural damage perspective, previous studies indicate that NIEL is much more dominant at keV energy range. A higher NIEL value in the perovskite photo-absorber suggests more crystalline damage, while IEL has demonstrated a competitive effect on NIEL by promoting healing effects in a variety of materials due to microscopic annealing along the ion track.[30–34] As shown in Figure 2, the NIEL value for the 20 keV protons is around 41 times greater as compared to the 1 MeV proton at the peak depth (~240 nm) in the perovskite layer. While the IEL value for the 20 keV incident proton is only ~1.3 times greater as compared to the 1 MeV proton. As a result, 20 keV

protons cause significantly more crystalline damage to the perovskite layer than 1 MeV protons.

Annual LEO fluences were estimated for 20 keV protons from Space Environment Information System (SPENVIS) simulations, with samples receiving cumulative proton doses spanning five orders of magnitude between 5×10^{10} and 1×10^{16} p$^+$/cm^2. Table 1 details the particle fluence received by each of the 12 samples in this study. Samples 1–4 were exposed to combinations of fast (4.5 MeV) and slow (<0.05 eV) neutrons prior to proton irradiation. "Low n^0" samples received a total dose of 2.76×10^5 mrem, while "high n^0" experienced 5.52×10^4 mrem, doses equivalent to 1 and 2 years on the lunar surface, respectively. After the first round of irradiation, select samples were exposed to further rounds of irradiation to capture possible non-linear damage mechanisms, with all samples fully characterized between each irradiation. Control samples were fabricated prior to each irradiation round to provide additional comparison. The control samples were shipped in the same vacuum-sealed package to the ion irradiation facility at the University of North Texas to account for the changes caused by the exposure to different laboratory environments.

Scanning electron and confocal microscopy

Figure 3 is a series of scanning electron microscopy (SEM) images of a control sample (Figure 3A) and those after proton exposure of fluences 10^{13}–10^{16} p$^+$/cm^2 (Figures 3B–3E). There were no obvious differences indicating degradation to the film morphology with increasing fluence, confirming what has been observed previously. However, SEM is not the best characterization platform as it does not allow direct pre- and post-irradiation comparison. Confocal microscopy imaging in Figure 4 maps the photoluminescence (PL) response of the films before and after each proton irradiation. Figures 4A–4C shows emission from sample #7 (Table 1) before radiation exposure, after the first irradiation with 10^{10} p$^+$/cm^2, and then after the second irradiation with 10^{13} p$^+$/cm^2. Figures 4D–4F are similar images of sample #4 prior to any exposure, and after second and third irradiations with fluences of 10^{12} and 10^{14} p$^+$/cm^2, respectively. While visually sample #7 images show very little difference, sample #4, unchanged at a fluence of 10^{12} p$^+$/cm^2, undergoes distinct darkening post-irradiation with 10^{14} p$^+$/cm^2, indicative of defect-induced non-radiative recombination. We quantified non-emissive areas across multiple confocal images (Figure S1) for both these samples and those exposed to higher fluences up to 1×10^{16} p$^+$/cm^2 using statistical analysis via ImageJ. Comparison of the proportion of darkened regions after irradiation in Figure 4G revealed that samples exposed to fluences > 10^{13} p$^+$/cm^2 all elicited comparable percentages of radiation-induced PL signal loss. Thus, even orders of magnitude differences in proton bombardment produced analogous PL deterioration and darkened film regions. This fluence-dependent damage indicates escalating non-radiative pathways through increasing radiation-induced trap state densities. In other words, there appears to be a threshold that proton fluence needs to exceed. Samples irradiated at fluences < 10^{14} p$^+$/cm^2 exhibited similar dark area changes of less than 5%. Similarly, the same analysis for samples #1 and #2 after neutron radiation shows no discernible changes (Figure S2), indicating high tolerance.
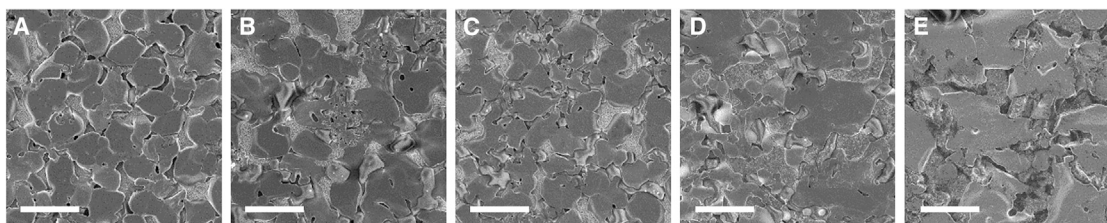
Figure 3. Scanning Electron Microscopy
(A) Control, and after proton exposure at (B) 10^{13} p$^+$/cm^2, (C) 10^{14} p$^+$/cm^2, (D) 10^{15} p$^+$/cm^2, (E) 10^{16} p$^+$/cm^2. Irradiated sample numbers 5, 8, 11, and 12, respectively. All scale bars are 10 μm.

Bandgap and lifetimes with increasing proton fluence

Following the confocal investigation, all samples were characterized via high-resolution scanning PL to fully characterize their spectral response, summarized in Figure 5. PL maps of 1 mm^2 areas on each film were used to calculate the average bandgap energy of all samples, including controls, and plotted across all fluences in Figure 5A (Figure S3). While samples receiving 10^{12} p$^+$/cm^2 experienced a negligible energy shift in comparison to the controls, fluences > 10^{13} p$^+$/cm^2 produced a linear blue shift with increasing value. Increasing proton exposure was also found to rapidly decrease the average charge recombination lifetime, depicted in Figure 5B. This reduction in charge recombination lifetime is expected. At this energy of 20 keV, protons generate substantial crystalline lattice defects before stopping inside the MHP layer. These collisions displace atoms and create vacancies and interstitials within. As exposure continues, defect densities increase which enables escalating non-radiative recombination through these mid-bandgap trap states. Optically, this also causes the decrease in photoluminescence emission intensity (the photodarkening described in Figure 4). The increase in the bandgap energy in CH$_3$NH$_3$PbI$_{3-x}$Cl$_x$ is usually indicative of chemical degradation typical in organic-inorganic halide perovskites,[24,35] which results in the formation of lead halide domains. These emit at lower wavelengths (higher energy), resulting in an overall spectral blue shift. The trend observed in Figure 5A is increased compositional dissociation within the film due to increased fluence, which also leads to spectral broadening (Figure 5C). There is an additional mechanism that could also contribute to a spectral blue-shift, originating in tensile strain.[24] However, that is not the likely cause here, as the results of light-soaking are confirmed in Figure 6.

AM1.5 light soaking

MHPs exhibit complex behavior under continuous light exposure, involving the interplay of defect formation, ion migration, and self-healing mechanisms. MHPs are susceptible to light-induced defect formation, including halide vacancies and interstitials, which enhance ion migration and increase defect density under prolonged illumination. Interestingly, the modest visible light intensity can sometimes reverse the damage and anneal away defects through the activation of innate ion migration transport properties in MHPs. Specifically, CH$_3$NH$_3^+$ cations and halide anions have been observed to fill vacancies, repair anti-site defects, and reconstruct the crystalline structure.[15] We compare the response to "light soaking" (LS) with

AM1.5 illumination for 15 h between proton-irradiated samples and a control film in Figure 6. Figures 6A and 6B illustrate the energy bandgap and the PL emission intensity changes over time, respectively. Initially, the proton-irradiated films displayed larger bandgaps compared to the non-irradiated control, indicating a higher baseline of disorder from radiation-induced defects. This observation aligns with the observation in Figure 5A where structural defects caused by increased proton irradiation result in blue-shifted emission and larger bandgaps due to increased disorder.

During LS, the control film progressed as anticipated, with gradual blue-shifting and dimming of PL emission over time. This behavior suggests progressive structural degradation and increasing defect density in the non-irradiated sample. In contrast, the irradiated samples, which started with notably blue-shifted PL peaks, showed little further spectral variation. This difference in behavior points to a potential balance between further degradation and self-healing mechanisms in the pre-damaged structures, while also confirming the strain-induced spectral changes observed in Figures 5A, as reported in prior studies,[24] is not the case here, as that was reversed by light soaking. Regarding emission intensity, the irradiated films initially darkened more rapidly than the control. This faster initial darkening could be attributed to the activation of existing defect sites in the irradiated samples. However, despite differing starting points and photodarkening extents, the spectral metrics converged to similar values for all three films in terms of both PL peak energy and intensity by the endpoint. This unexpected equivalent convergence is particularly surprising given the substantially higher photodarkening the control exhibits over the irradiation-disordered samples, as calculated from the confocal images (Figure S4) and plotted in Figure 6C. The convergence of spectral properties suggests that the systems may reach a similar equilibrium state regardless of initial defect concentrations. This equilibrium could represent a balance between ongoing defect formation and dynamic repair processes mediated by light-activated ion migration. The resistance of irradiated samples to further spectral changes might indicate a saturation of certain types of defects or a dynamic equilibrium where defect formation and repair rates balance out more quickly in pre-damaged structures.

Notably, there were no signs of light-induced healing typically associated with strain relaxation in the perovskite film.[24] This absence of strain-related healing is consistent with the experimental conditions, as without thermal cycling or constraining
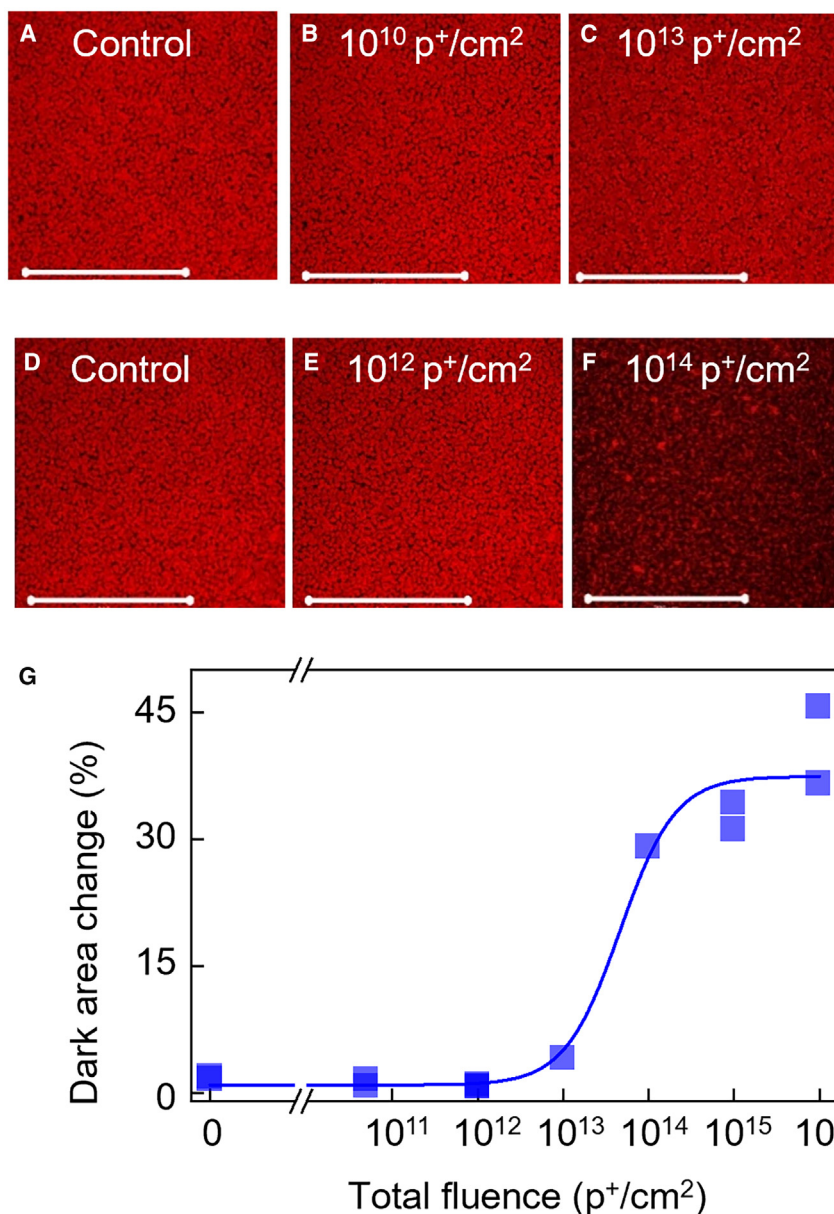
Figure 4. Confocal Microscopy
Confocal fluorescence images of sample 7 (A) before irradiation, (B) after the first irradiation, and (C) after the second irradiation.
(D–F) Same protocol for sample 4. Scale bars: 200 μm.
(G) Change in percent non-emissive area post-irradiation for all proton fluences tested.

comparable levels of non-radiative recombination and darkened fractional areas. This threshold aligns with linear blue-shifting and charge lifetime reductions observed in the 10^{14}–10^{16} p^+/cm^2 regime, confirming increasing defect densities that enable non-radiative pathways. Bandgap widening stems from chemical degradation and dissociation. Subsequent visible light exposure and prolonged light soaking reveal some divergence between the photostability trends of pristine, and irradiated films.
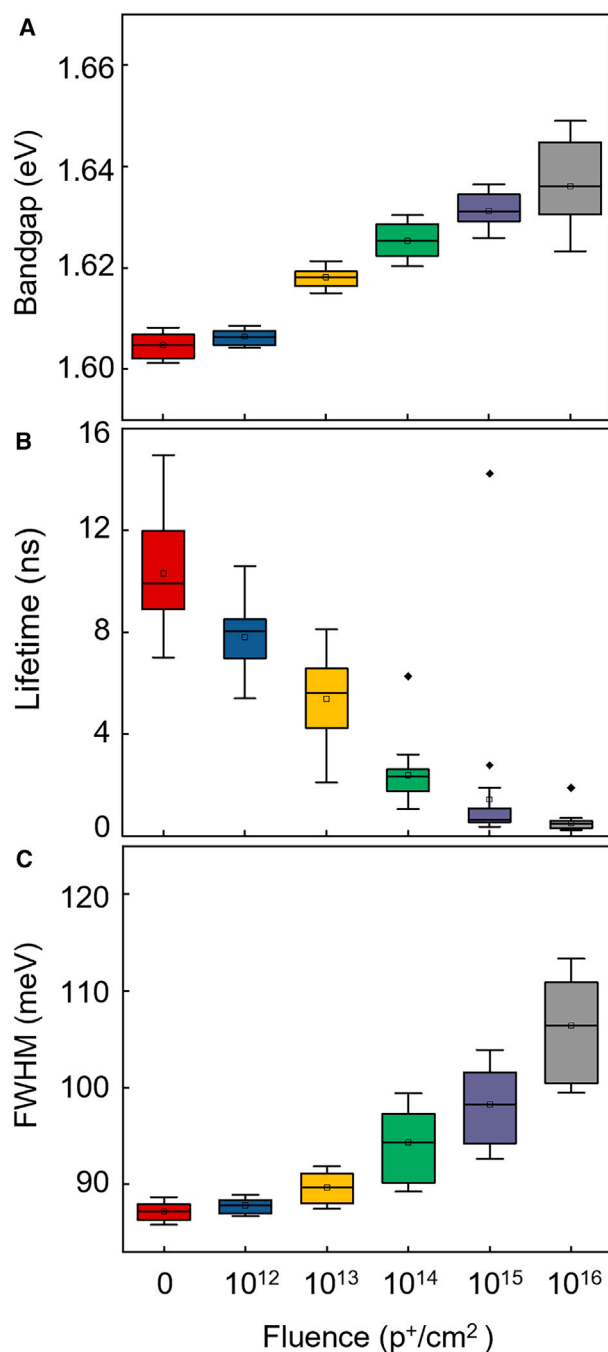
Finally, our studies confirm that spectral characterization is superior to traditional photovoltaic power measurements in revealing true proton radiation tolerance limits. Optical metrics exposed damage beginning at proton fluences of 10^{13} p^+/cm^2 whereas prior work has not seen any degradation from space-relevant proton energies manifest in full solar cell PCE until higher fluences.[18,20] Furthermore, PCE depends strongly on initial device quality, masking incremental damage in poor-performing films.[30] Full device encapsulation and interfaces also convolute damage localization. Thus, traditional electrical tests fail to sensitively convey fundamental radiation tolerance. In contrast, direct optical probing of the bare absorber layer alone provides straightforward, intrinsic insights on defect generation and lower fluence damage onset undetectable electrically. Eliminating confounding factors from other layers or low baseline PCE enables straightforward interpretation on proton bombardment impacts through sensitive photoluminescence (PL), bandgap, and lifetime metrics. However, PL alone is not comprehensive, and the combination of techniques we have employed, including confocal microscopy and scanning electron microscopy alongside PL spectroscopy allowed us to correlate spectral changes with morphological and structural alterations at various scales, providing a more nuanced view of radiation-induced damage. This multimodal optical spectroscopy and imaging on isolated films thereby constitutes the most revealing approach for accurately assessing proton radiation degradation in metal halide perovskites.

layers on top of the perovskite film, it is unlikely that the samples experienced any significant stress.[36] This observation suggests that the observed phenomena are primarily driven by light-induced defect dynamics rather than strain-related effects.

DISCUSSION

This optical characterization of proton-irradiated perovskite thin films provides strong data in support of their radiation tolerance and the possibility of recovery under AM1.5 light soaking. The results demonstrate that the proton irradiation of methylammonium lead halide perovskite films generates escalating radiation damage at fluences exceeding 10^{13} p^+/cm^2, as quantified through decreasing PL emission intensity. All higher fluences produce

Figure 5. Bandgap and lifetimes with increasing proton fluence
Boxplots depicting (A) band gap, (B) charge recombination lifetime, and (C) spectral full width half maximum averaged over all samples for each radiation fluence. Data are represented as mean ± SD.

Limitations of the study

This systematic study effectively establishes key radiation response mechanisms, though several aspects warrant further investigation. While the use of ITO-coated glass substrates enabled clear measurements, the potential PL quenching effects suggest value in exploring additional substrate configurations to
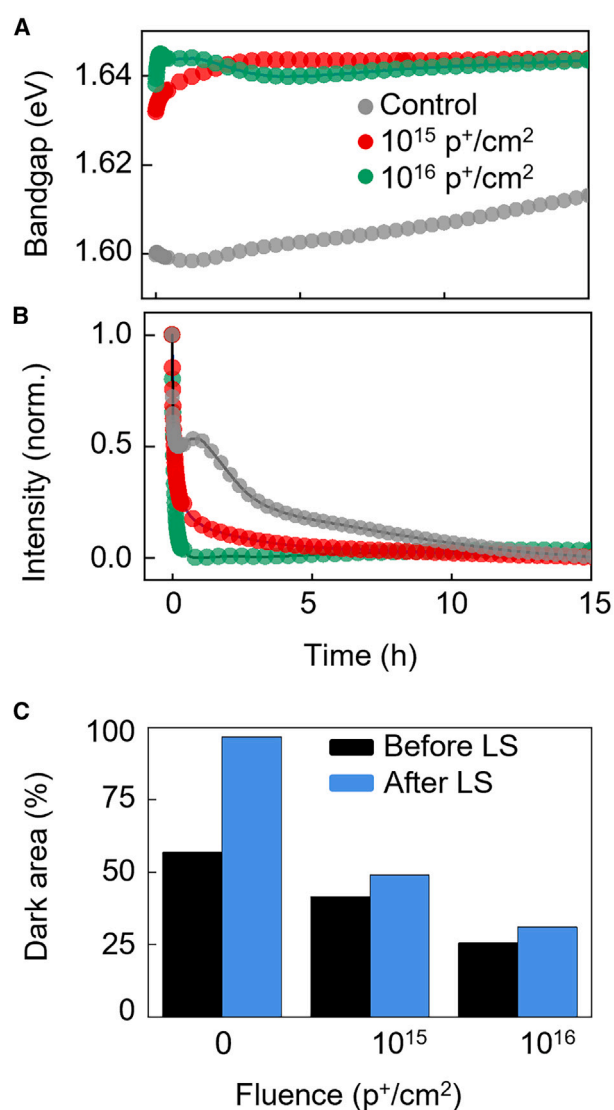
Figure 6. AM1.5 light soaking
(A) Energy, and (B) PL intensity measured over 15 h of AM1.5 illumination, comparing a control sample with two irradiated with 10^{15} and 10^{16} p$^+$/cm^2.
(C) Percent non-emissive area before and after light-soaking for the same samples.

fully represent device architectures. The research focuses on $CH_3NH_3PbI_{3-x}Cl_x$ (x = 0.15) composition while providing crucial insights, and indicates opportunities to examine how compositional variations might affect radiation tolerance. Though the selection of 20 keV proton energy through SRIM/TRIM simulations was well-justified, understanding responses across a broader radiation energy spectrum would strengthen space-application feasibility. The controlled laboratory conditions, while essential for isolating specific effects, do not fully capture the complex interplay of simultaneous space environment stressors. Additionally, while our study establishes important radiation tolerance thresholds, extending observation time frames could better align with actual space mission durations. These

limitations, rather than detracting from the value of this study, highlight promising directions for building upon this strong methodological foundation.

RESOURCE AVAILABILITY

Lead contact

Further information and requests for resources should be directed to and will be fulfilled by the lead contact, Sayantani Ghosh (sghosh@ucmerced.edu).

Materials availability

This study did not generate new unique material.

Data and code availability

- Data: The SRIM simulation data and photoluminescent spectra have been provided in the article.
- Code: The Python codes used for post-analysis in this article can be provided upon reasonable request.
- All other requests: Any additional information required to reanalyze the data reported will be shared by the lead contact upon request.

AUTHOR CONTRIBUTIONS

S.E. and C.L. initiated the project, performed optical characterization, and analyzed data. K.S. and C.L. performed neutron irradiation of samples. M.P. and D.K.S. performed proton irradiation of samples. B.R., C.P., T.P., L.M., and S.G. supervised the project and discussed data. The article was written by S.E. and S.G., with contributions from all authors.

DECLARATION OF INTERESTS

The authors declare no competing interests.

STAR★METHODS

Detailed methods are provided in the online version of this paper and include the following:

- KEY RESOURCES TABLE
- METHOD DETAILS
  - Thin film fabrication
  - Irradiation
  - Stopping range of ions in matter (SRIM) calculation information
  - Confocal microscopy
  - Photoluminescence spectroscopy
  - AM 1.5 stability
- QUANTIFICATION AND STATISTICAL ANALYSIS

SUPPLEMENTAL INFORMATION

Supplemental information can be found online at https://doi.org/10.1016/j.isci.2024.111586.

REFERENCES

1. Tu, Y., Wu, J., Xu, G., Yang, X., Cai, R., Gong, Q., Zhu, R., and Huang, W. (2021). Perovskite Solar Cells for Space Applications: Progress and Challenges. Adv. Mater. *33*, 2006545. https://doi.org/10.1002/adma.202006545.

2. Hoang, M.T., Yang, Y., Tuten, B., and Wang, H. (2022). Are Metal Halide Perovskite Solar Cells Ready for Space Applications? J. Phys. Chem. Lett. *13*, 2908–2920. https://doi.org/10.1021/acs.jpclett.2c00386.

3. Best Research-Cell Efficiency Chart. https://www.nrel.gov/pv/cell-efficiency.html.

4. Kang, S., Jeong, J., Cho, S., Yoon, Y.J., Park, S., Lim, S., Kim, J.Y., and Ko, H. (2019). Ultrathin, lightweight and flexible perovskite solar cells with an excellent power-per-weight performance. J. Mater. Chem. A *7*, 1107–1114. https://doi.org/10.1039/C8TA10585E.

5. Bailey, S., and Raffaelle, R. (2012). Chapter IID-2 - Operation of Solar Cells in a Space Environment. In Practical Handbook of Photovoltaics, Second Edition, A. McEvoy, T. Markvart, and L. Castañer, eds. (Academic Press), pp. 863–880. https://doi.org/10.1016/B978-0-12-385934-1.00027-1.

6. Sahoo, D., Sahoo, S., Alagarasan, D., Ganesan, R., Varadharajaperumal, S., and Naik, R. (2022). Proton Ion Irradiation on As40Se50Sb10 Thin Films: Fluence-Dependent Tuning of Linear–Nonlinear Optical Properties for Photonic Applications. ACS Appl. Electron. Mater. *4*, 856–868. https://doi.org/10.1021/acsaelm.1c01223.

7. Priyadarshini, P., Alagarasan, D., Ganesan, R., Varadharajaperumal, S., and Naik, R. (2023). Influence of Proton Ion Irradiation on the Linear–Nonlinear Optoelectronic Properties of $Sb_{40}Se_{20}S_{40}$ Thin Films at Different Fluences for Photonic Devices. ACS Appl. Opt. Mater. *1*, 55–68. https://doi.org/10.1021/acsaom.2c00007.

8. Paternò, G.M., Robbiano, V., Santarelli, L., Zampetti, A., Cazzaniga, C., Sakai, V.G., and Cacialli, F. (2019). Perovskite solar cell resilience to fast neutrons. Sustain. Energy Fuels *3*, 2561–2566. https://doi.org/10.1039/C9SE00102F.

9. Haviland, H.F., Bertone, P.F., Christl, M.J., Caffrey, J.A., and Apple, J.A. (2020). Artemis III Neutron Surface Science.

10. Townsend, L.W. (2020). Space weather on the Moon. Phys. Today *73*, 66–67. https://doi.org/10.1063/PT.3.4438.

11. Reitz, G., Berger, T., and Matthiae, D. (2012). Radiation exposure in the moon environment. Planet. Space Sci. *74*, 78–83. https://doi.org/10.1016/j.pss.2012.07.014.

12. Zhang, S., Wimmer-Schweingruber, R.F., Yu, J., Wang, C., Fu, Q., Zou, Y., Sun, Y., Wang, C., Hou, D., Böttcher, S.I., et al. (2020). First measurements of the radiation dose on the lunar surface. Sci. Adv. *6*, eaaz1334. https://doi.org/10.1126/sciadv.aaz1334.

13. Pérez-del-Rey, D., Dreessen, C., Igual-Muñoz, A.M., van den Hengel, L., Gélvez-Rueda, M.C., Savenije, T.J., Grozema, F.C., Zimmermann, C., and Bolink, H.J. (2020). Perovskite Solar Cells: Stable under Space Conditions. Sol. RRL *4*, 2000447. https://doi.org/10.1002/solr.202000447.

14. Herrera Martínez, W.O., Correa Guerrero, N.B., Gómez Andrade, V.A., Alurralde, M., and Perez, M.D. (2022). Evaluation of the resistance of halide perovskite solar cells to high energy proton irradiation for space applications. Sol. Energy Mater. Sol. Cells *238*, 111644. https://doi.org/10.1016/j.solmat.2022.111644.

15. Huang, J.-S., Kelzenberg, M.D., Espinet-González, P., Mann, C., Walker, D., Naqavi, A., Vaidya, N., Warmann, E., and Atwater, H.A. (2017). Effects of Electron and Proton Radiation on Perovskite Solar Cells for Space Solar Power Application. In 2017 IEEE 44th Photovoltaic Specialist Conference (PVSC), pp. 1248–1252. https://doi.org/10.1109/PVSC.2017.8366410.

16. Kanaya, S., Kim, G.M., Ikegami, M., Miyasaka, T., Suzuki, K., Miyazawa, Y., Toyota, H., Osonoe, K., Yamamoto, T., and Hirose, K. (2019). Proton Irradiation Tolerance of High-Efficiency Perovskite Absorbers for Space Applications. J. Phys. Chem. Lett. *10*, 6990–6995. https://doi.org/10.1021/acs.jpclett.9b02665.

17. Malinkiewicz, O., Imaizumi, M., Sapkota, S.B., Ohshima, T., and Öz, S. (2020). Radiation effects on the performance of flexible perovskite solar cells for space applications. Emergent Mater. *3*, 9–14. https://doi.org/10.1007/s42247-020-00071-8.

18. Miyazawa, Y., Ikegami, M., Chen, H.-W., Ohshima, T., Imaizumi, M., Hirose, K., and Miyasaka, T. (2018). Tolerance of Perovskite Solar Cell to High-Energy Particle Irradiations in Space Environment. iScience *2*, 148–155. https://doi.org/10.1016/j.isci.2018.03.020.

19. He, J., Li, T., Liu, X., Su, H., Ku, Z., Zhong, J., Huang, F., Peng, Y., and Cheng, Y.-B. (2019). Influence of phase transition on stability of perovskite solar cells under thermal cycling conditions. Sol. Energy *188*, 312–317. https://doi.org/10.1016/j.solener.2019.06.025.

20. Costa, C., Manceau, M., Duzellier, S., Nuns, T., and Cariou, R. (2023). Perovskite solar cells under protons irradiation: From in-situ IV-monitoring to root cause degradation elucidation. Sol. Energy Mater. Sol. Cells *257*, 112388. https://doi.org/10.1016/j.solmat.2023.112388.

21. Reb, L.K., Böhmer, M., Predeschly, B., Grott, S., Weindl, C.L., Ivandekic, G.I., Guo, R., Dreißigacker, C., Gernhäuser, R., Meyer, A., and Müller-Buschbaum, P. (2020). Perovskite and Organic Solar Cells on a Rocket Flight. Joule *4*, 1880–1892. https://doi.org/10.1016/j.joule.2020.07.004.

22. Cardinaletti, I., Vangerven, T., Nagels, S., Cornelissen, R., Schreurs, D., Hruby, J., Vodnik, J., Devisscher, D., Kesters, J., D'Haen, J., et al. (2018). Organic and perovskite solar cells for space applications. Sol. Energy Mater. Sol. Cells *182*, 121–127. https://doi.org/10.1016/j.solmat.2018.03.024.

23. Tu, Y., Xu, G., Yang, X., Zhang, Y., Li, Z., Su, R., Luo, D., Yang, W., Miao, Y., Cai, R., et al. (2019). Mixed-cation perovskite solar cells in space. Sci. China Phys. Mech. Astron. *62*, 974221. https://doi.org/10.1007/s11433-019-9356-1.

24. Delmas, W., Erickson, S., Arteaga, J., Woodall, M., Scheibner, M., Krause, T.S., Crowley, K., VanSant, K.T., Luther, J.M., Williams, J.N., et al. (2023). Evaluation of Hybrid Perovskite Prototypes After 10 Month Space Flight on the International Space Station. Adv. Energy Mater. *13*, 2203920. https://doi.org/10.1002/aenm.202203920.

25. McMillon-Brown, L., Luther, J.M., and Peshek, T.J. (2022). What Would It Take to Manufacture Perovskite Solar Cells in Space? ACS Energy Lett. *7*, 1040–1042. https://doi.org/10.1021/acsenergylett.2c00276.

26. Jamshaid, A., Guo, Z., Hieulle, J., Stecker, C., Ohmann, R., Ono, L.K., Qiu, L., Tong, G., Yin, W., and Qi, Y. (2021). Atomic-scale insight into the enhanced surface stability of methylammonium lead iodide perovskite by controlled deposition of lead chloride. Energy Environ. Sci. *14*, 4541–4554. https://doi.org/10.1039/D1EE01084K.

27. Bouchard, M., Hilhorst, J., Pouget, S., Alam, F., Mendez, M., Djurado, D., Aldakov, D., Schülli, T., and Reiss, P. (2017). Direct Evidence of Chlorine-Induced Preferential Crystalline Orientation in Methylammonium Lead Iodide Perovskites Grown on TiO2. J. Phys. Chem. C *121*, 7596–7602. https://doi.org/10.1021/acs.jpcc.6b11529.

28. Miyazawa, Y., Ikegami, M., Miyasaka, T., Ohshima, T., Imaizumi, M., and Hirose, K. (2015). Evaluation of radiation tolerance of perovskite solar cell for use in space. In 2015 IEEE 42nd Photovoltaic Specialist Conference (PVSC), pp. 1–4. https://doi.org/10.1109/PVSC.2015.7355859.

29. Lang, F., Nickel, N.H., Bundesmann, J., Seidel, S., Denker, A., Albrecht, S., Brus, V.V., Rappich, J., Rech, B., Landi, G., and Neitzert, H.C. (2016). Radiation Hardness and Self-Healing of Perovskite Solar Cells. Adv. Mater. *28*, 8726–8731. https://doi.org/10.1002/adma.201603326.

30. Kirmani, A.R., Byers, T.A., Ni, Z., VanSant, K., Saini, D.K., Scheidt, R., Zheng, X., Kum, T.B., Sellers, I.R., McMillon-Brown, L., et al. (2024). Unraveling radiation damage and healing mechanisms in halide perovskites using energy-tuned dual irradiation dosing. Nat. Commun. *15*, 696. https://doi.org/10.1038/s41467-024-44876-1.

31. Durant, B.K., Afshari, H., Singh, S., Rout, B., Eperon, G.E., and Sellers, I.R. (2021). Tolerance of perovskite solar cells to targeted proton irradiation and electronic ionization induced healing. ACS Energy Lett. *6*, 2362–2368. https://doi.org/10.1021/acsenergylett.1c00756.

32. Chacon, S.A., Khanal, M.N., Durant, B.K., Afshari, H., Byers, T.A., Parashar, M., Rout, B., Whiteside, V.R., Poplavskyy, D., and Sellers, I.R. (2024). Probing the Interfacial Properties of ACIGS Solar Cells with Targeted Proton Irradiation. Sol. RRL *8*, 2300756. https://doi.org/10.1002/solr.202300756.

33. Das, S., Senapati, S., Alagarasan, D., Ganesan, R., Varadharajaperumal, S., and Naik, R. (2023). Modifications in the structural, morphological, optical properties of Ag45Se40Te15 thin films by proton ion irradiation for optoelectronics and nonlinear applications. Ceram. Int. *49*, 10319–10331. https://doi.org/10.1016/j.ceramint.2022.11.212.

34. Panda, R., Rath, H., Khan, S.A., Alagarasan, D., Singh, U.P., Mishra, N.C., and Naik, R. (2023). Interface engineered nanostructured phase formation at Se/In sites by Ag ion irradiation and its structural, optical and morphological behavior. Surface. Interfac. *40*, 103081. https://doi.org/10.1016/j.surfin.2023.103081.

35. Choi, H., Ke, J.C.R., Skalsky, S., Castle, C.A., Li, K., Moore, K.L., Flavell, W.R., and Parkinson, P. (2020). Visualizing the role of photoinduced ion migration on photoluminescence in halide perovskite grains. J. Mater. Chem. C *8*, 7509–7518. https://doi.org/10.1039/D0TC01441A.

36. Krause, T.S., VanSant, K.T., Lininger, A., Crowley, K., Peshek, T.J., and McMillon-Brown, L. (2023). Thermal Performance of Perovskite-Based Photovoltaics for Operation in Low Earth Orbit. Sol. RRL *7*, 2300468. https://doi.org/10.1002/solr.202300468.

37. Kirmani, A.R., Durant, B.K., Grandidier, J., Haegel, N.M., Kelzenberg, M.D., Lao, Y.M., McGehee, M.D., McMillon-Brown, L., Ostrowski, D.P., Peshek, T.J., et al. (2022). Countdown to perovskite space launch: Guidelines to performing relevant radiation-hardness experiments. Joule *6*, 1015–1031. https://doi.org/10.1016/j.joule.2022.03.004.

38. Rout, B., Dhoubhadel, M.S., Poudel, P.R., Kummari, V.C., Pandey, B., Deoli, N.T., Lakshantha, W.J., Mulware, S.J., Baxley, J., Manuel, J.E., et al. (2013). An overview of the facilities, activities, and developments at the University of North Texas Ion Beam Modification and Analysis Laboratory (IBMAL). AIP Conf. Proc. *1544*, 11–18. https://doi.org/10.1063/1.4813454.

STAR★METHODS

KEY RESOURCES TABLE

REAGENT or RESOURCE	SOURCE	IDENTIFIER
Chemicals, peptides, and recombinant proteins		
Perovskite Precursor Ink for Nitrogen Processing	Osilla	I201 (https://www.ossila.com/products/perovskite-ink-nitrogen?variant=1200243997)
Software and algorithms		
SRIM/TRIM		http://www.srim.org/

METHOD DETAILS

Thin film fabrication

All samples were fabricated at the University of California, Merced between November 2022 and March 2023. The perovskite precursor solution was purchased from Ossila ("Perovskite Precursor Ink for Air Processing") and consisted of 3:1 methylammonium iodide to lead chloride in dimethylformamide. Films were deposited on ITO glass substrates by spin coating 50 μL of ink at 3000 rpm for 30 s, then annealing at 90°C for 35 min on a hotplate. X-ray photoelectron spectroscopy was used to determine the iodide to chloride ratio in the final perovskite crystal. For $CH_3NH_3PbI_{3-x}Cl_x$, 'x' was measured as 0.15. Samples were stored in the dark in vacuum bags packed with desiccant after fabrication.

Irradiation

The proton irradiations were performed in the Ion beam laboratory at the University of North Texas. 20 keV proton beams were generated from the TiH cathode by using Source of Negative Ion by Cesium Sputtering (SNICS-II, NEC).[37,38] Proton beam was raster scanned over the region of interest using an electrostatic raster scanner for uniform irradiation in the low energy irradiation chamber. All irradiations were performed in the vacuum chamber under a vacuum of 1×10^{-7} torr. The neutron irradiations were performed at NASA Langley Research Center using Am/Be (1 Curie) neutron source to generate fast neutrons (4.5 MeV).

Stopping range of ions in matter (SRIM) calculation information

The range and collision profile of the energetic protons in the samples were simulations by using the SRIM ion-solid interaction software package using 100,000 ions with the following layer details; perovskite: 600 nm, 4.286 g/cm³; ITO: 100 nm, 7.14 g/cm³; borosilicate glass: 200 nm, 2.23 g/cm³. The glass was kept at such a narrow width to speed calculations but was nominally 1 mm thick.

Confocal microscopy

A Zeiss LSM 880 confocal microscope was used before and after irradiation tests to image reflection and emission from samples. A 458 nm laser was used for excitation; reflection was filtered between 450 – 466 nm and PL was filtered between 750 – 800 nm.

Photoluminescence spectroscopy

Samples were excited at 532 nm with a repetition rate of 15.6 MHz using an NKT Photonics SuperK acousto-optic laser system. High-resolution spatial PL maps were constructed from each sample using a 100x Olympus objective and two Newport 300 translation stages controlled by a custom LabVIEW program. Emitted light from the samples was filtered by a 715 long pass filter before entering the spectrometer (Princeton Instruments Acton 2300). The spectrometer utilized a 500 nm blaze grating with 300 lines/mm to diffract the light onto the CCD camera. For time-resolved maps, the PL signal entered a PicoQuant single-photon avalanche diode.

AM 1.5 stability

Samples were continuously illuminated for 15 h at AM1.5 (Newport LSH-7320 ABA LED Solar Simulator) and PL was measured every 5 min. A 680 short pass filter was used to filter the simulated sunlight before reaching the sample. A 715 long pass filter was used below the sample to remove sunlight and collect the PL through the substrate. PL was transmitted via fiber optic cable into a spectrometer (Princeton Instruments Acton 2300).

QUANTIFICATION AND STATISTICAL ANALYSIS

All of the statistical details of experiments can be found summarized in Figure S3 and its caption, including the statistical method, number of data points for each sample, number of samples averaged for data reported in Figure 5.